Science Advances

AAAS

advances.sciencemag.org/cgi/content/full/3/3/e1601159/DC1

Supplementary Materials for

Assembly of mesoscale helices with near-unity enantiomeric excess and light-matter interactions for chiral semiconductors

Wenchun Feng, Ji-Young Kim, Xinzhi Wang, Heather A. Calcaterra, Zhibei Qu, Louisa Meshi, Nicholas A. Kotov

Published 1 March 2017, *Sci. Adv.* **3**, e1601159 (2017)
DOI: 10.1126/sciadv.1601159

The PDF file includes:

- fig. S24. Simulations using CdTe NP refractive index.
- schematic S1. Experimental methods.
- schematic S2. Schematic drawing of an “untwisted” helix
- table S1. Statistical analysis of racemic NP assemblies.
- table S2. Statistical analysis of geometrical parameters of helices obtained from SEM images.
- table S3. Percent yield calculations.
- section S1. Percent yield
- Legends for movies S1 to S6

Other Supplementary Material for this manuscript includes the following:
(available at advances.sciencemag.org/cgi/content/full/3/3/e1601159/DC1)

- movie S1 (.mp4 format). R-helix in 3D rotating view.
- movie S2 (.mp4 format). L-helix in 3D rotating view.
- movie S3 (.mp4 format). RCP irradiation on an R-helix.
- movie S4 (.mp4 format). RCP irradiation on an L-helix.
- movie S5 (.mp4 format). RCP irradiation on an achiral ribbon.
- movie S6 (.mp4 format). LCP irradiation on an achiral ribbon.

SUPPLEMENTARY MATERIALS

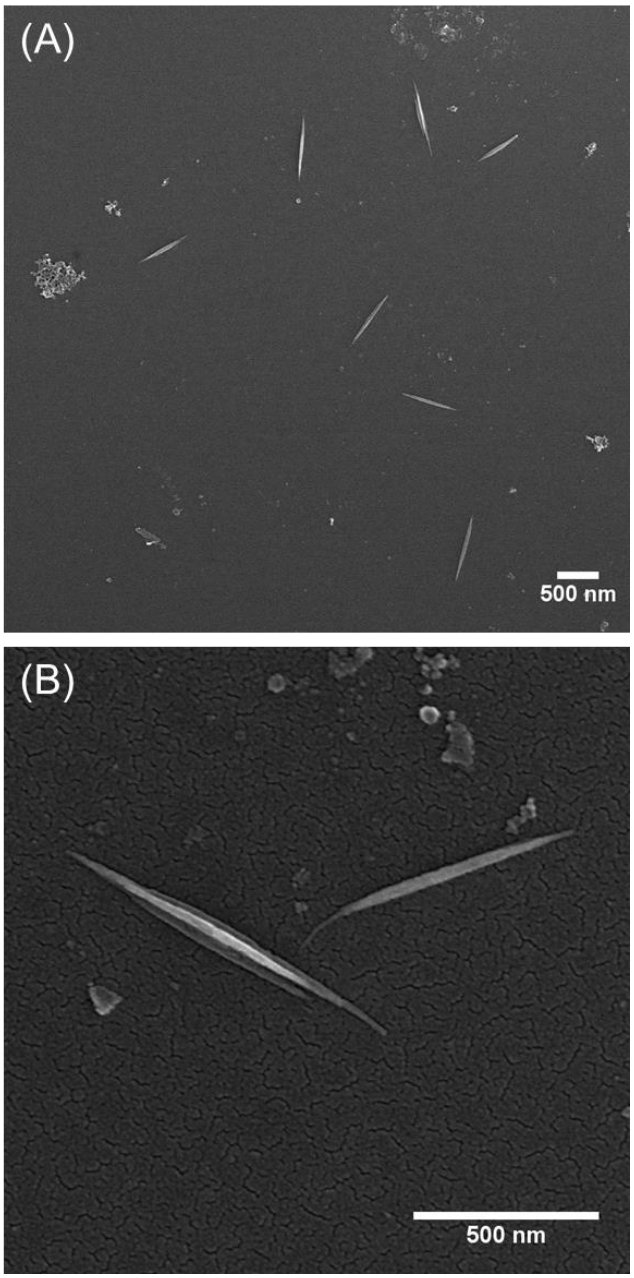

fig. S1. Assembly from TGA-CdTe NPs. SEM images of assemblies from achiral TGA-CdTe NPs, at different magnifications.

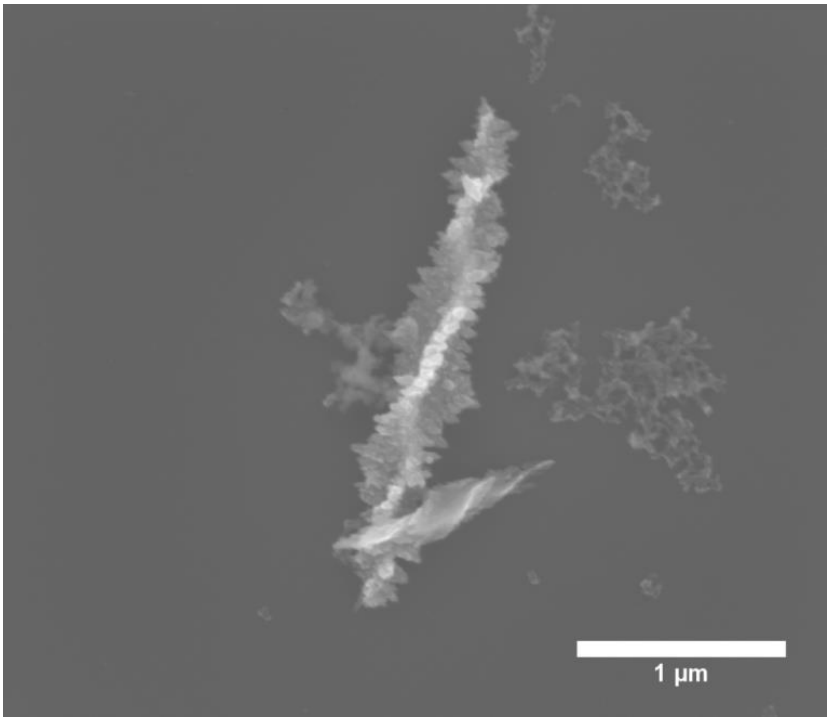

fig. S2. Helical structure of opposite handedness found among helices assembled from L-Cys CdTe NPs. A regular helix to its bottom right serves as a comparison in morphologies.

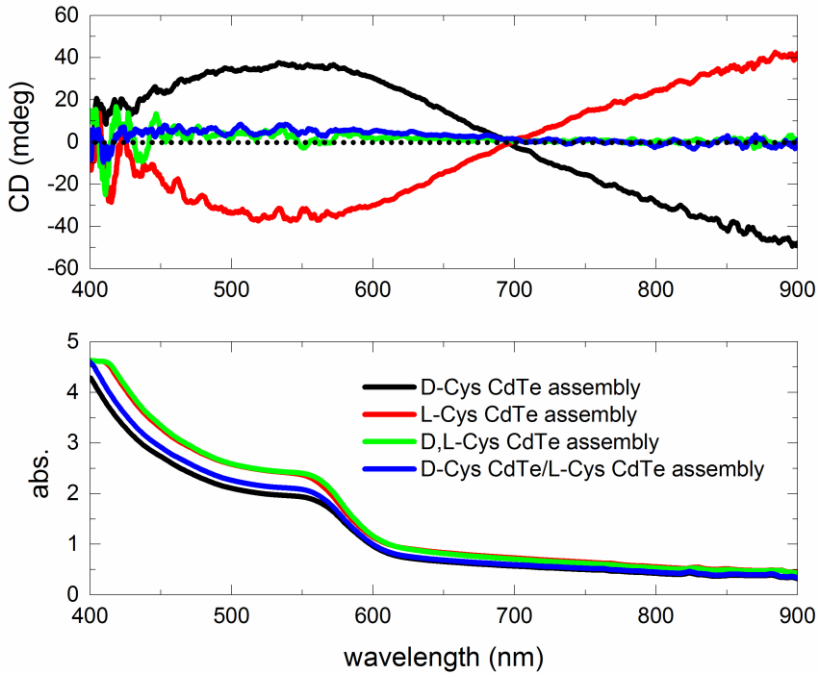

fig. S3. Chiroptical spectra of different NP assemblies.

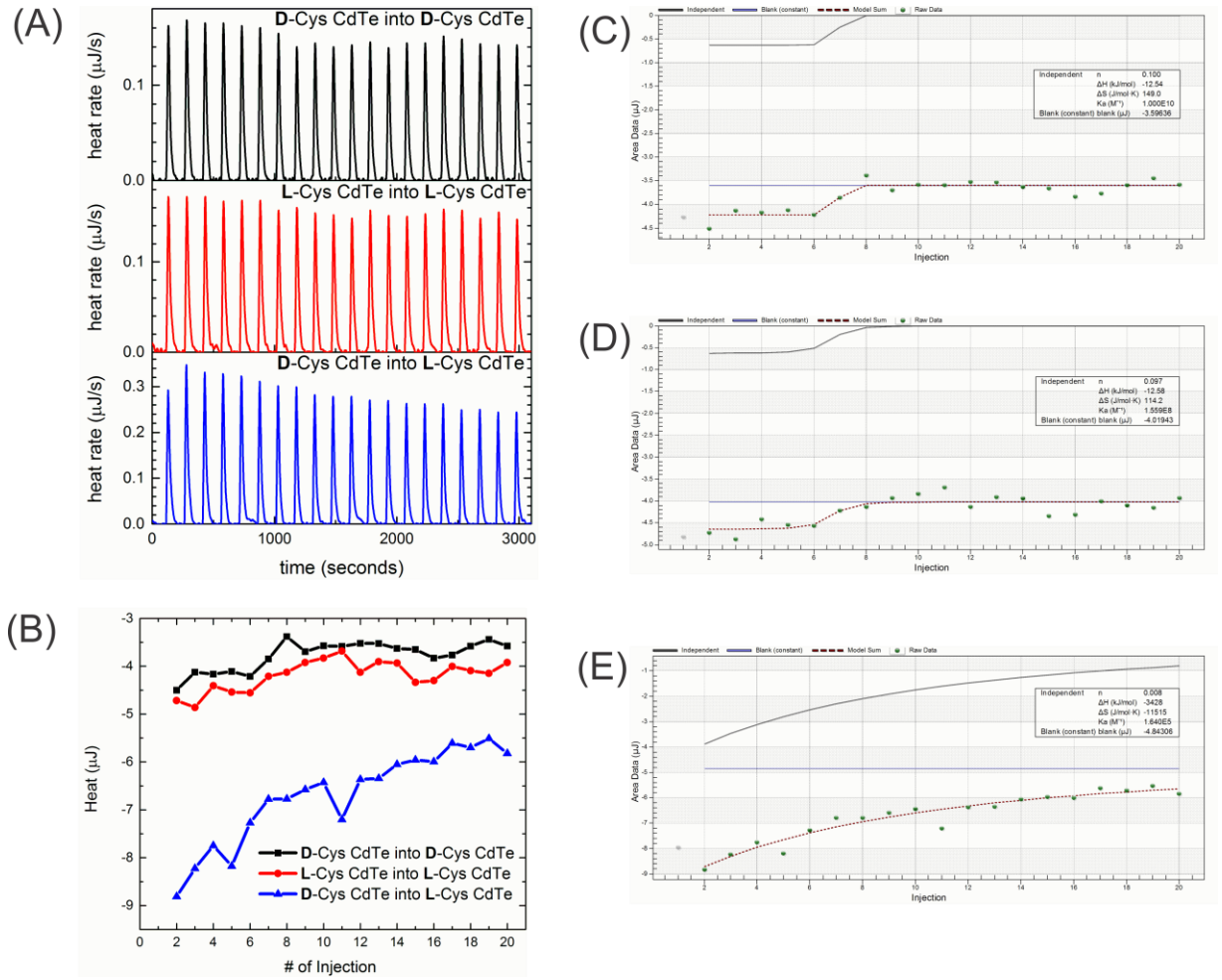

fig. S4. ITC data for chiral interactions and their fitting with thermodynamic models. (**A**) Heat rate and (**B**) total heat (integration of peak area) per injection. The first (small volume) injection is discarded. Modeling of (**C**) D-Cys CdTe into D-Cys CdTe, (**D**) L-Cys CdTe into L-Cys CdTe, and (**E**) D-Cys CdTe into L-Cys CdTe. It should be noted that the non-sigmoidal curve shape in (E) presents uncertainty in the determination of binding stoichiometry. For this fitting, we allowed the binding stoichiometry to freely vary during fitting and obtained the thermodynamics with binding stoichiometry = 0.008 and ΔG = -29 kJ/mol. If we assume that the actual binding stoichiometry is higher at 0.100 (the same binding stoichiometry as in the cases of D-Cys into D-Cys and L-Cys into L-Cys), best-fit ΔG becomes -32 kJ/mol, similar to that obtained with no restraints on binding stoichiometry. Therefore, the non-sigmoidal curve shape does not significantly impact the ΔG value determined from ITC data.

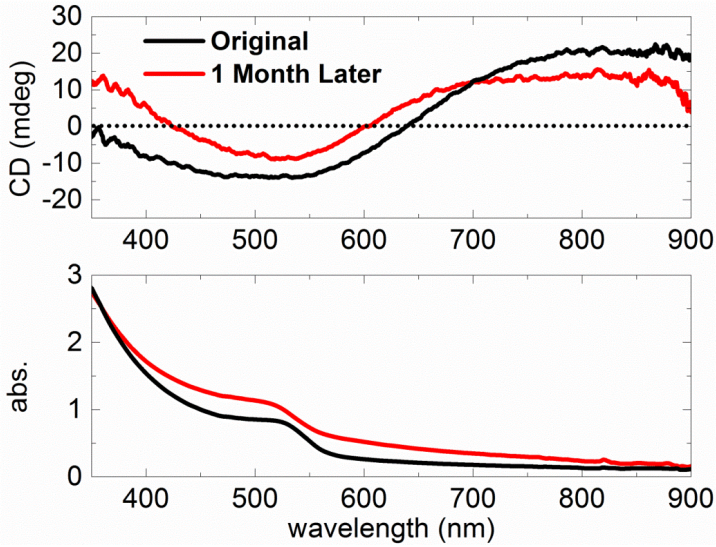

fig. S5. Long-term stability of homochiral mesoscale helices. CD and absorbance spectra of an L-Cys CdTe assembly, in the original state and after 1 month of storage at 4 °C in the dark.

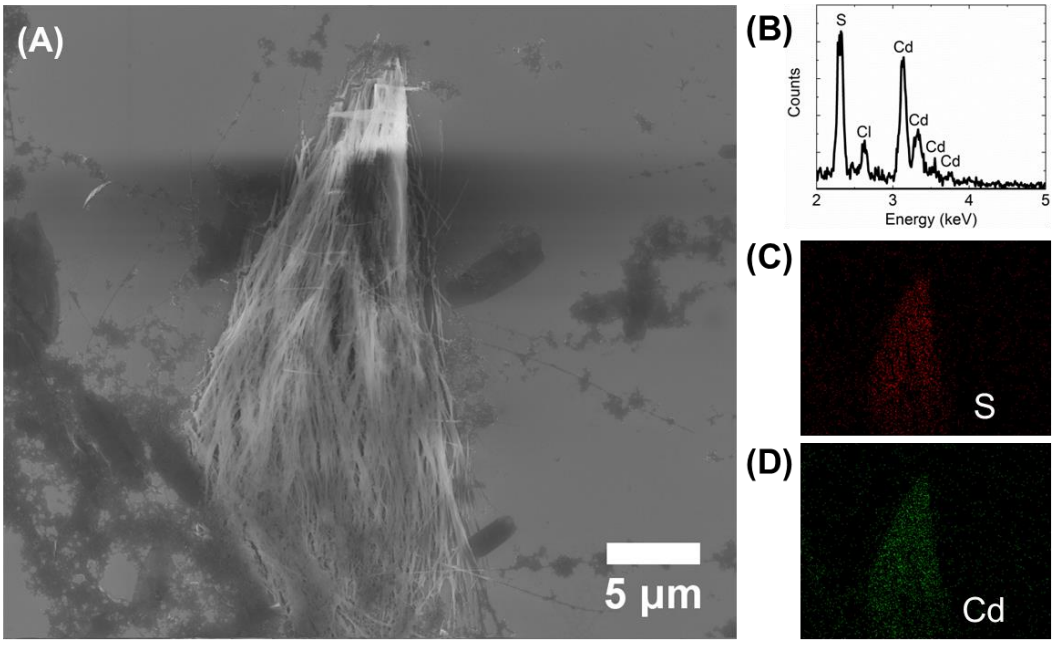

fig. S6. CdS nanofibers observed after long-term storage of the CdTe NP dispersions. (**A**) SEM image of bundled CdS fibers forming after 1 month of storage at 4 °C in the dark. As a comparison of size and morphology, note the one helix to the left of the bundle in bright contrast. (**B**) SEM-EDX spectrum showing the presence of Cd, S and Cl (Cl is from the starting material cysteine hydrochloride). Note the absence of Te signal in the range of ~3.7−4.7 keV. (**C**) Elemental mapping of S. (**D**) Elemental mapping of Cd.

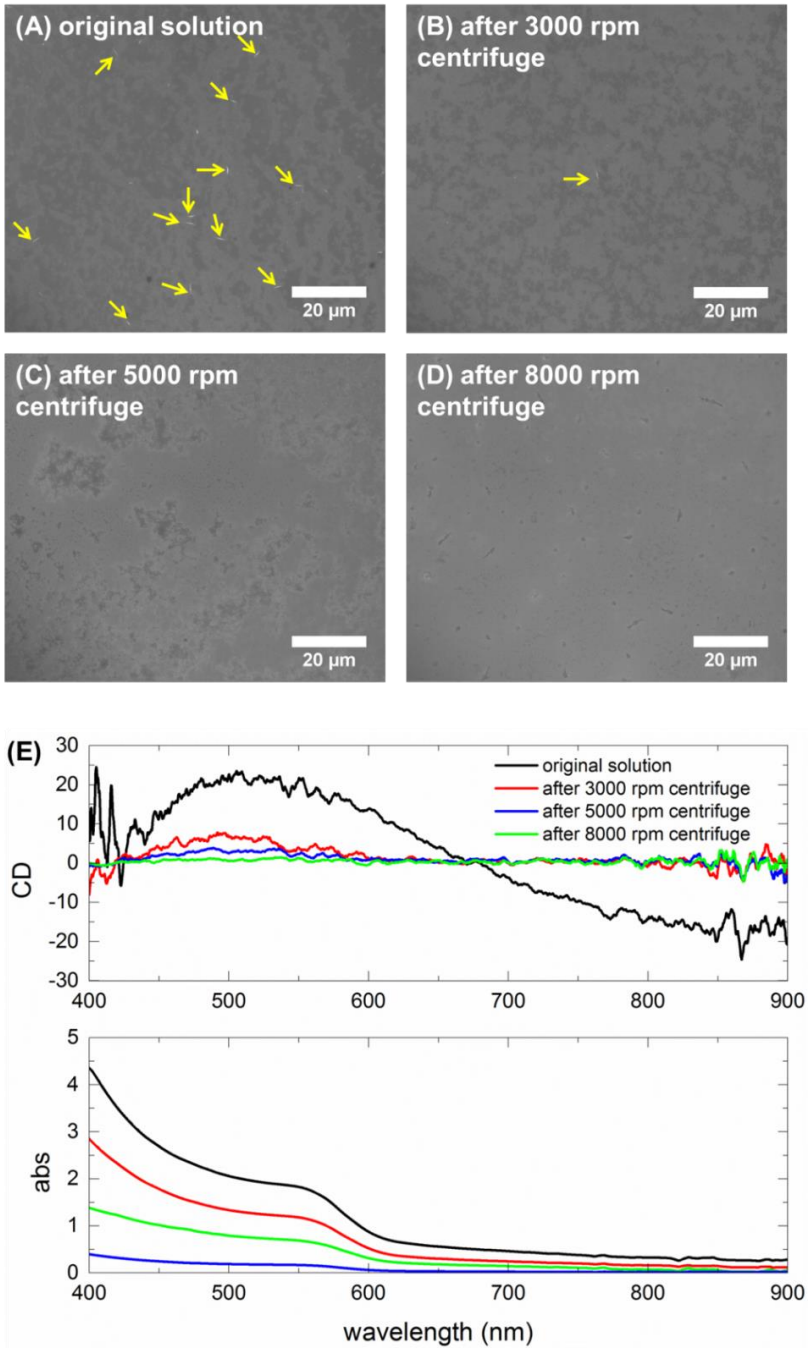

fig. S7. Contribution of random aggregates to the overall chiroptical activity. SEM images of (**A**) original assemblies, as well as after (**B**) 3000 rpm centrifugation, (**C**) 5000 rpm centrifugation, and (**D**) 8000 rpm centrifugation. Yellow arrows point to the helices. (**E**) CD and absorption spectra of the corresponding dispersions. The helices present in the original dispersions were mostly removed after centrifugation at 3000 rpm. Subsequent centrifugations of higher speeds reduced the volume density of the random aggregates.

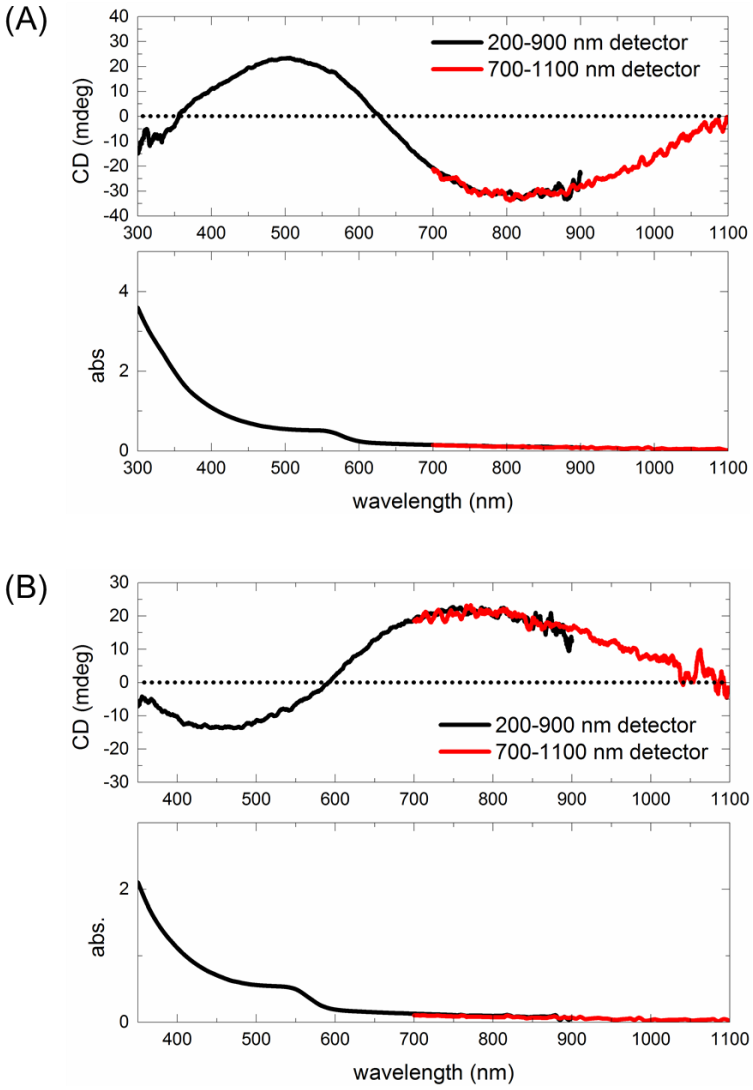

fig. S8. Vis-NIR chiroptical response of mesoscale helices. CD and absorbance spectra of (**A**) D-Cys CdTe and (**B**) L-Cys CdTe assemblies in water, using two separate detectors on a Jasco J-815 CD spectrophotometer.

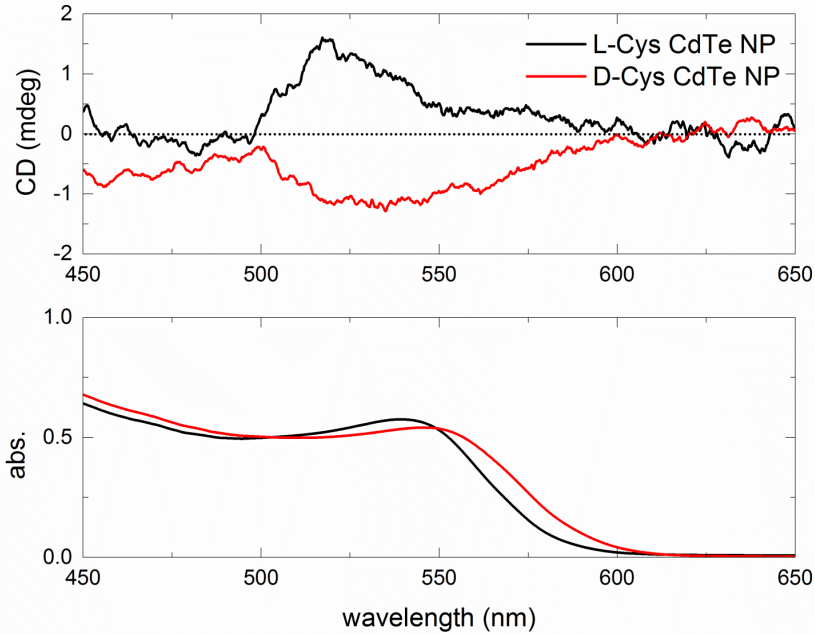

fig. S9. CD and absorption spectra of CdTe NPs.

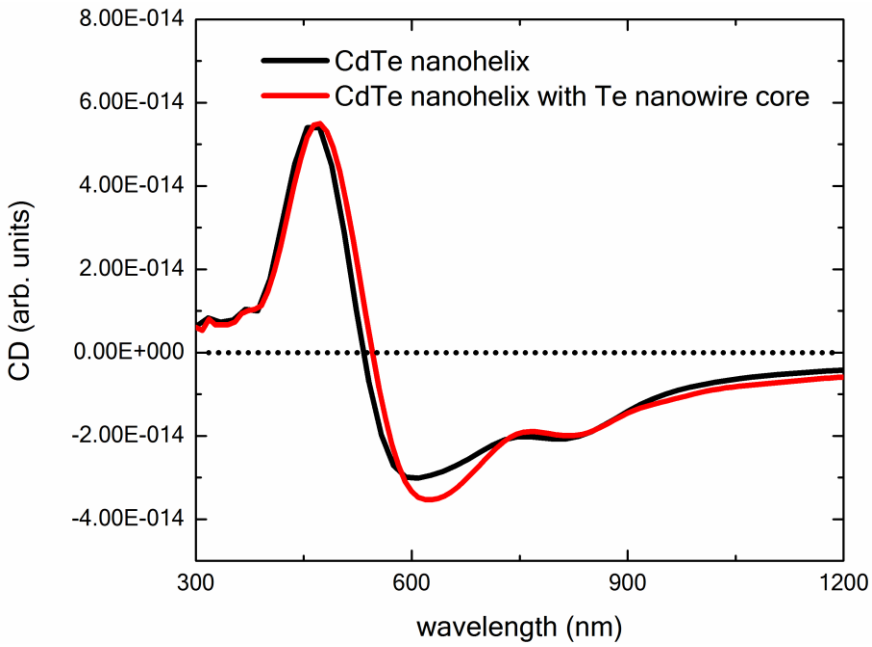

fig. S10. Calculated CD spectra of CdTe helix with or without a Te nanowire core. Comparison of simulated CD spectra of a CdTe helix with and without a Te nanowire core (nanowire diameter is the same as the thickness of the helix, nanowire geometry follows the rotation of the helix through the center).

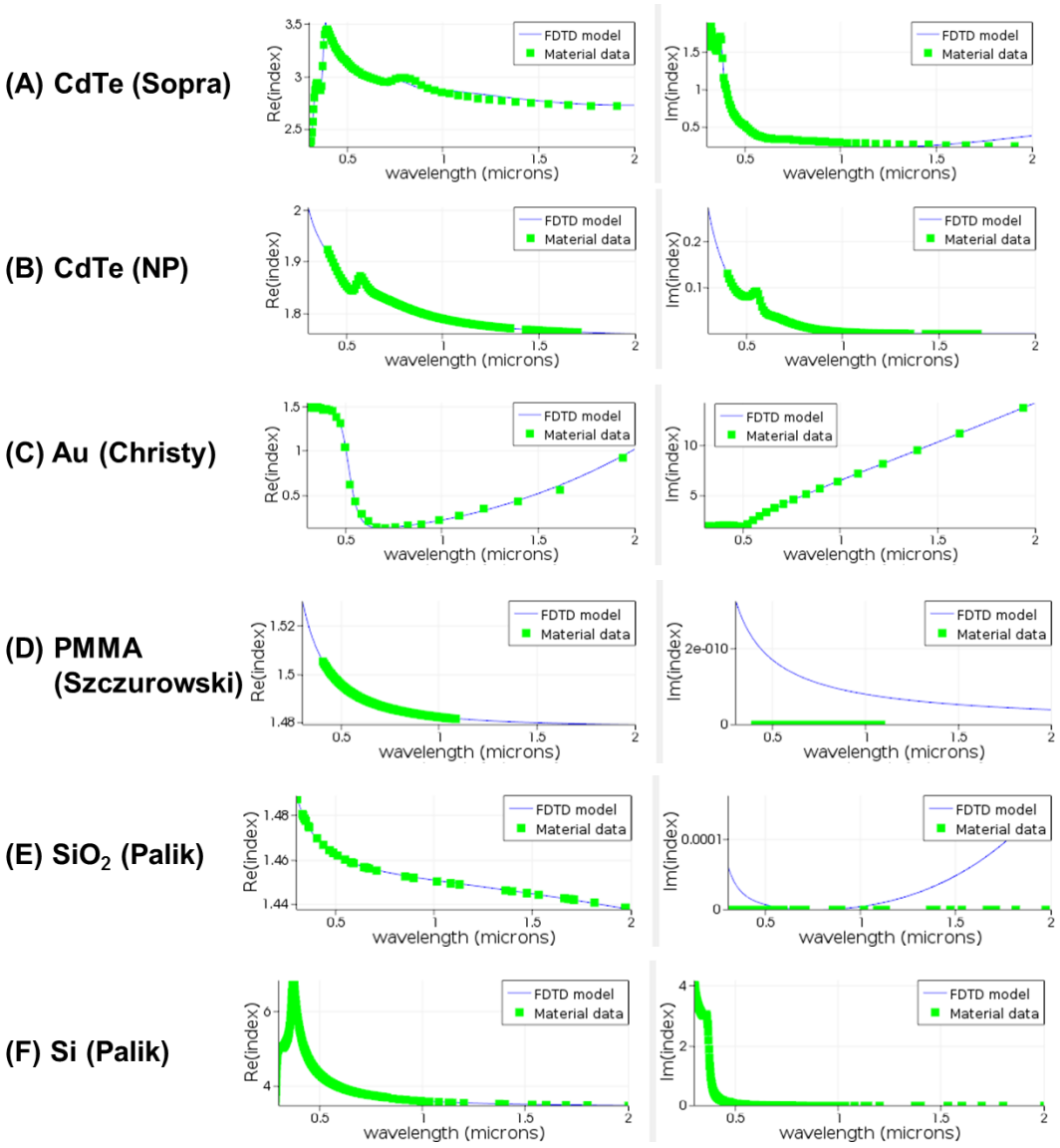

fig. S11. Refractive index data sets. Real and imaginary parts of the refractive index for (**A**) CdTe (Sopra Material Database), (**B**) CdTe (nanoparticle dataset), (**C**) Au (Johnson and Christy, Lumerical) (**D**) PMMA (Szczurowski, 2013), (**E**) SiO_2 (Palik, Lumerical) and (**F**) Si (Palik, Lumerical). The FDTD model fitting is shown alongside the original dataset. Note that the FDTD fitting of the imaginary refractive index of PMMA and SiO_2 does not adhere to the zero value reflected in the original dataset. This is due to a limitation of the fitting model for zero imaginary refractive index materials. A closer look reveals a very small residual for these fittings (below 10^{-4}), indicating that a good fit is indeed accomplished.

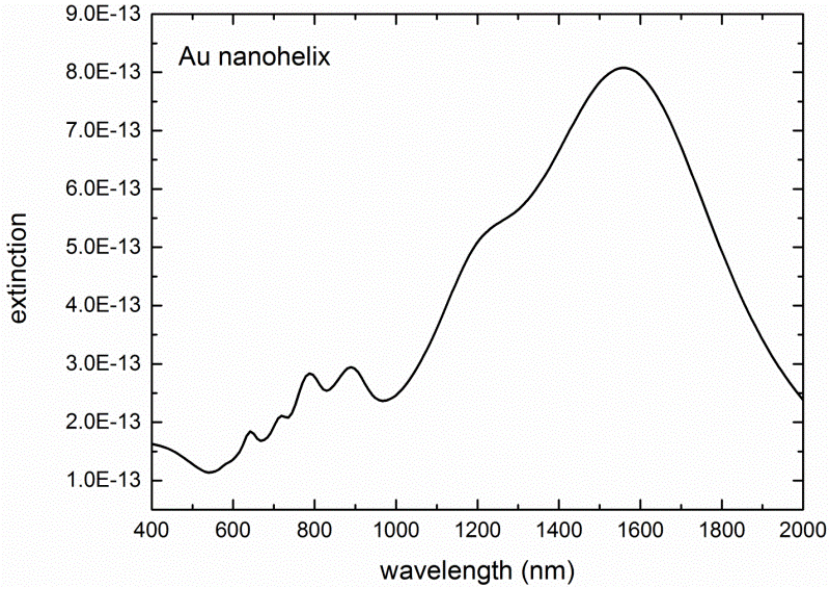

fig. S12. Extinction spectrum of Au helices.

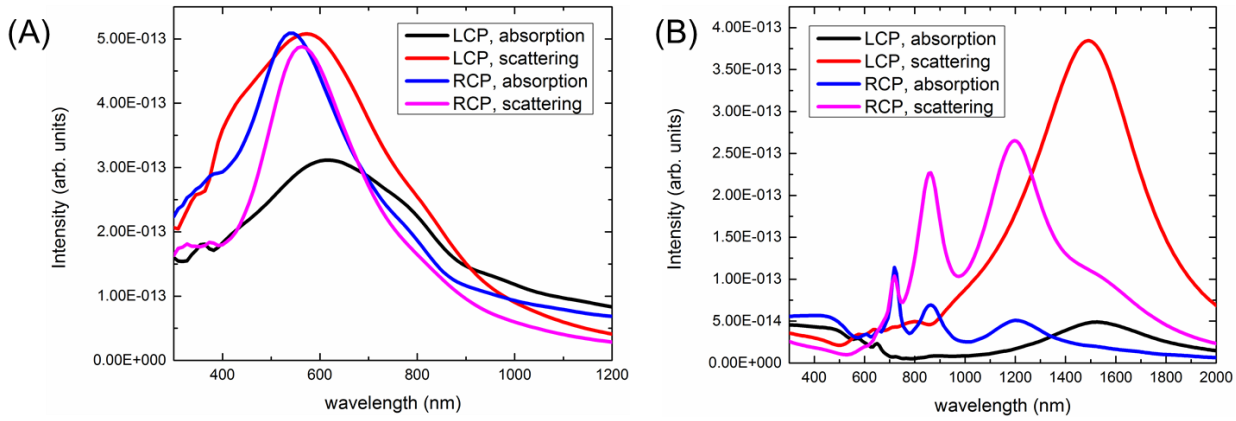

fig. S13. Absorption and scattering spectra of Au and CdTe helices. Absorption and scattering spectra of (**A**) CdTe and (**B**) Au helices under LCP and RCP irradiation.

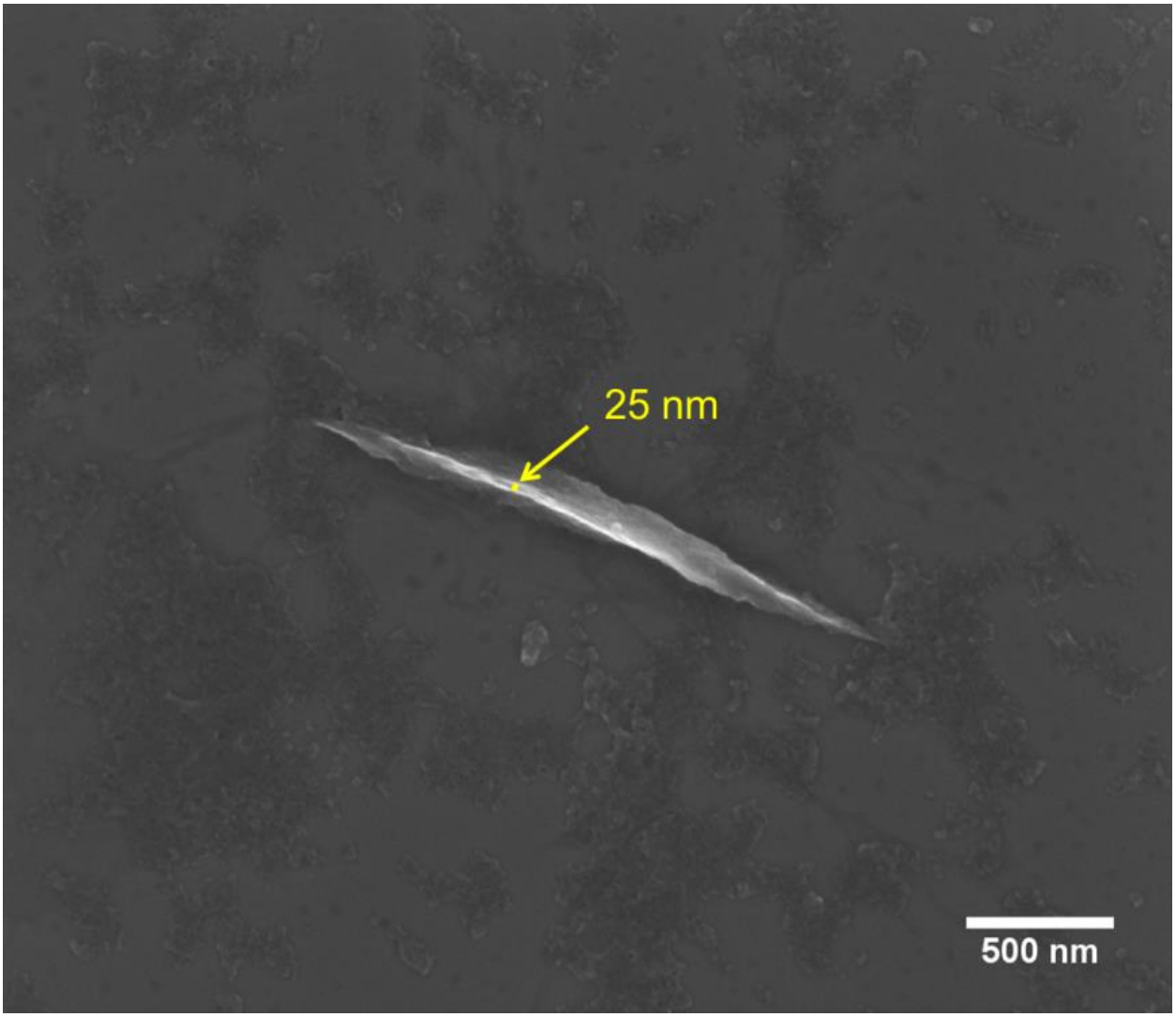

fig. S14. Helix thickness. SEM image of an R-helix with thickness highlighted and measured.

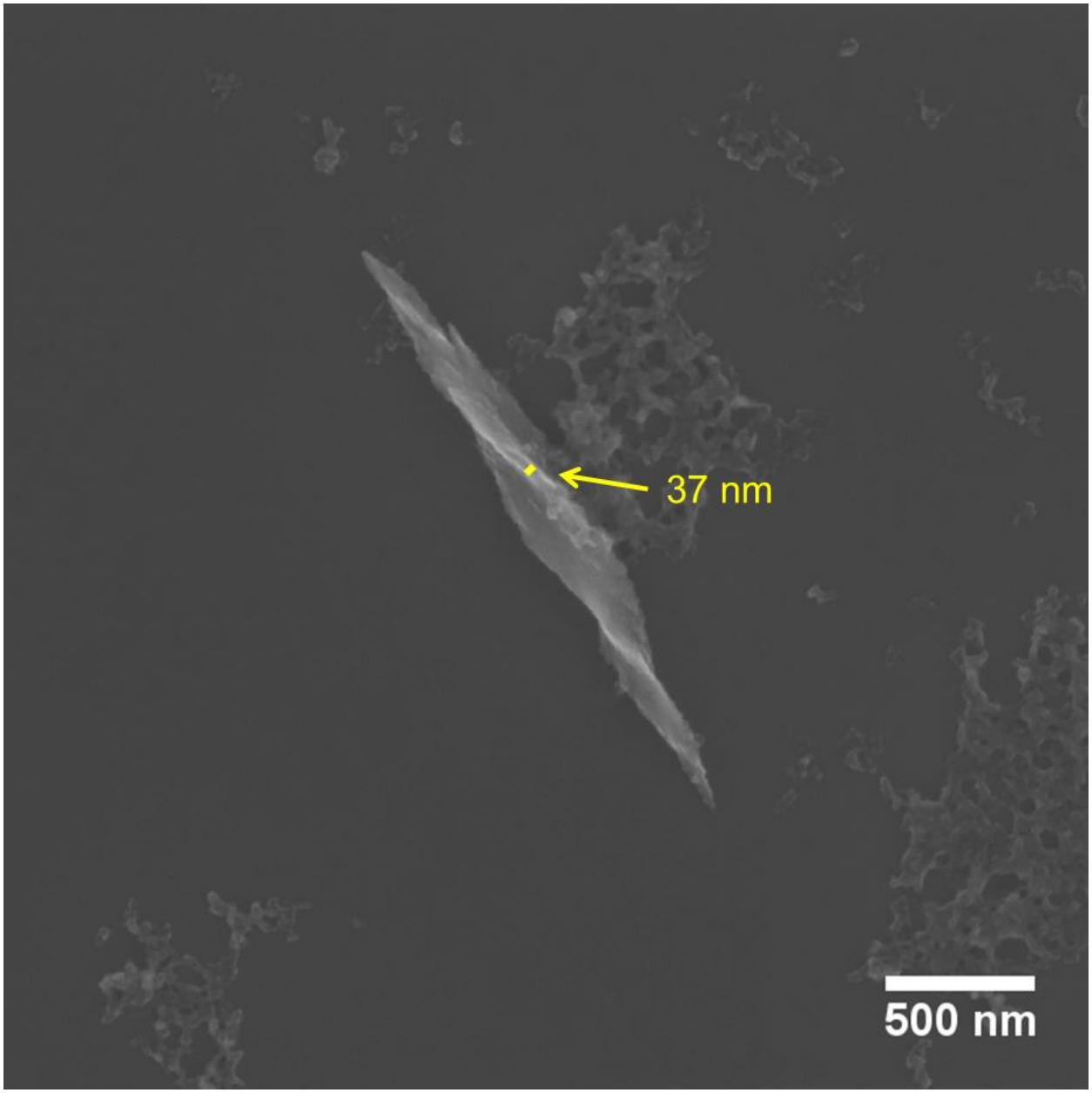

fig. S15. Helix thickness. SEM image of an L-helix with thickness highlighted and measured.

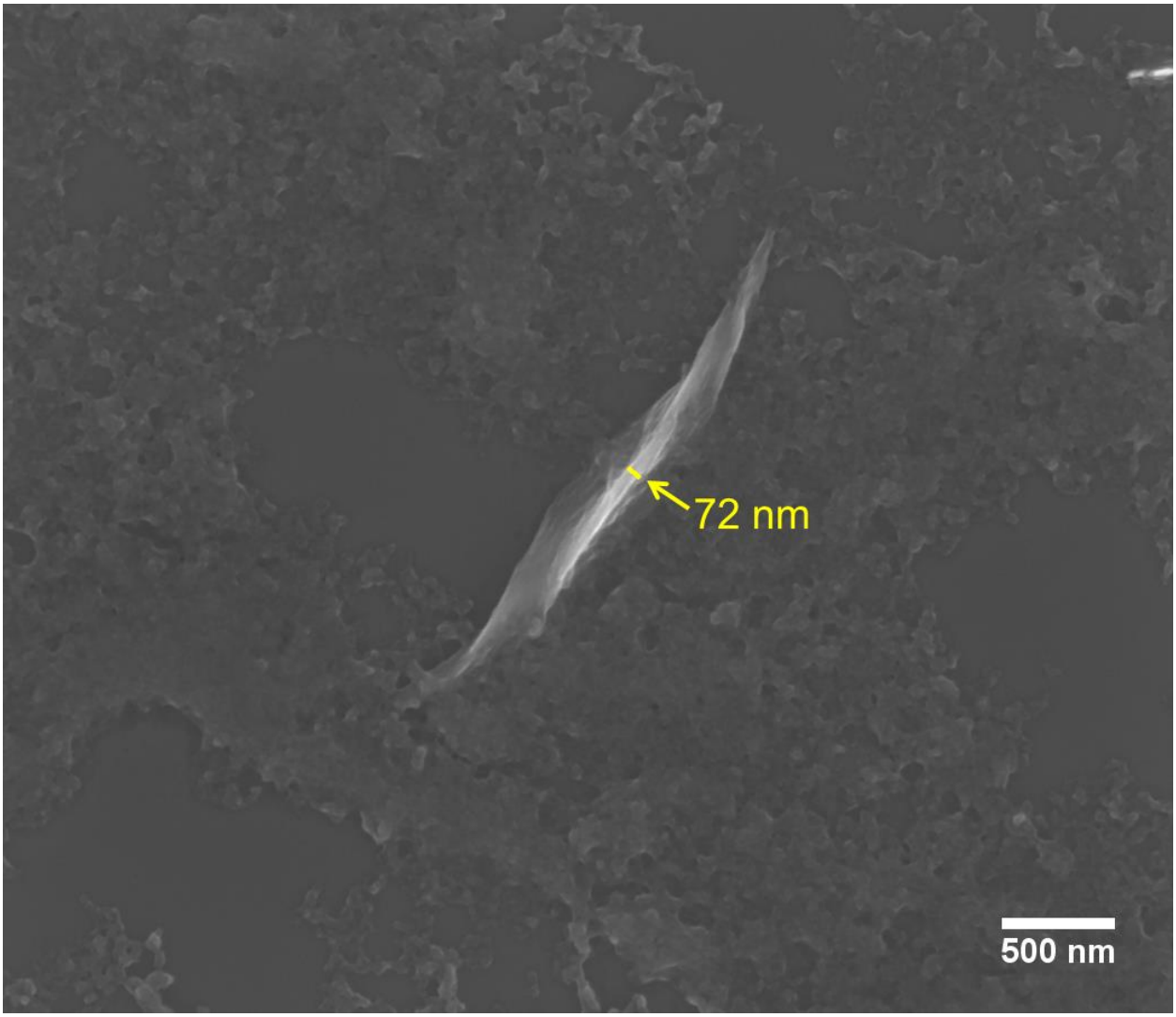

fig. S16. Helix thickness. SEM image of an L-helix with thickness highlighted and measured.

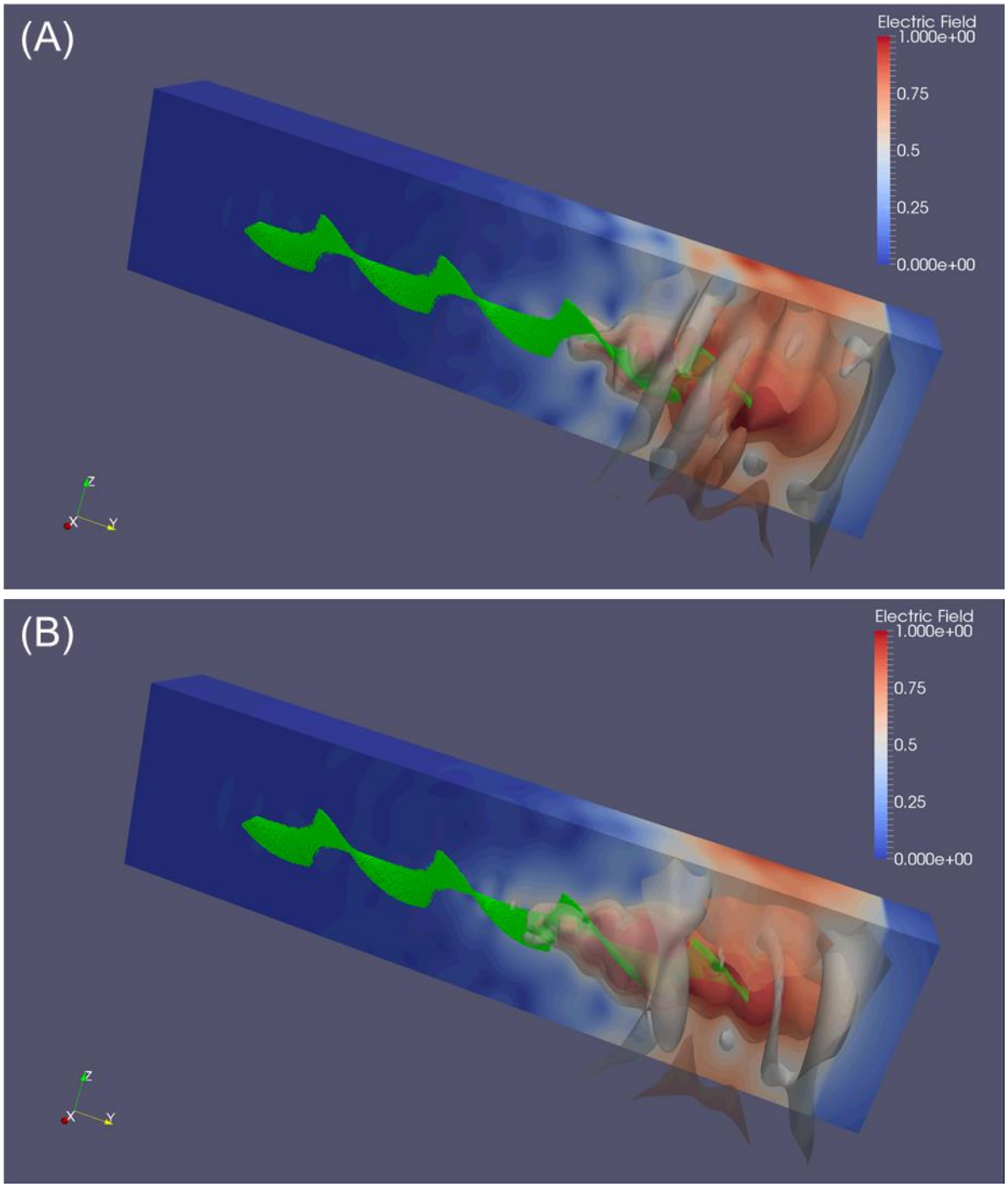

fig. S17. EFI movie snapshots. Electric field isosurface (EFI) movie snapshots with (**A**) LCP and (**B**) RCP irradiation of an R-helix.

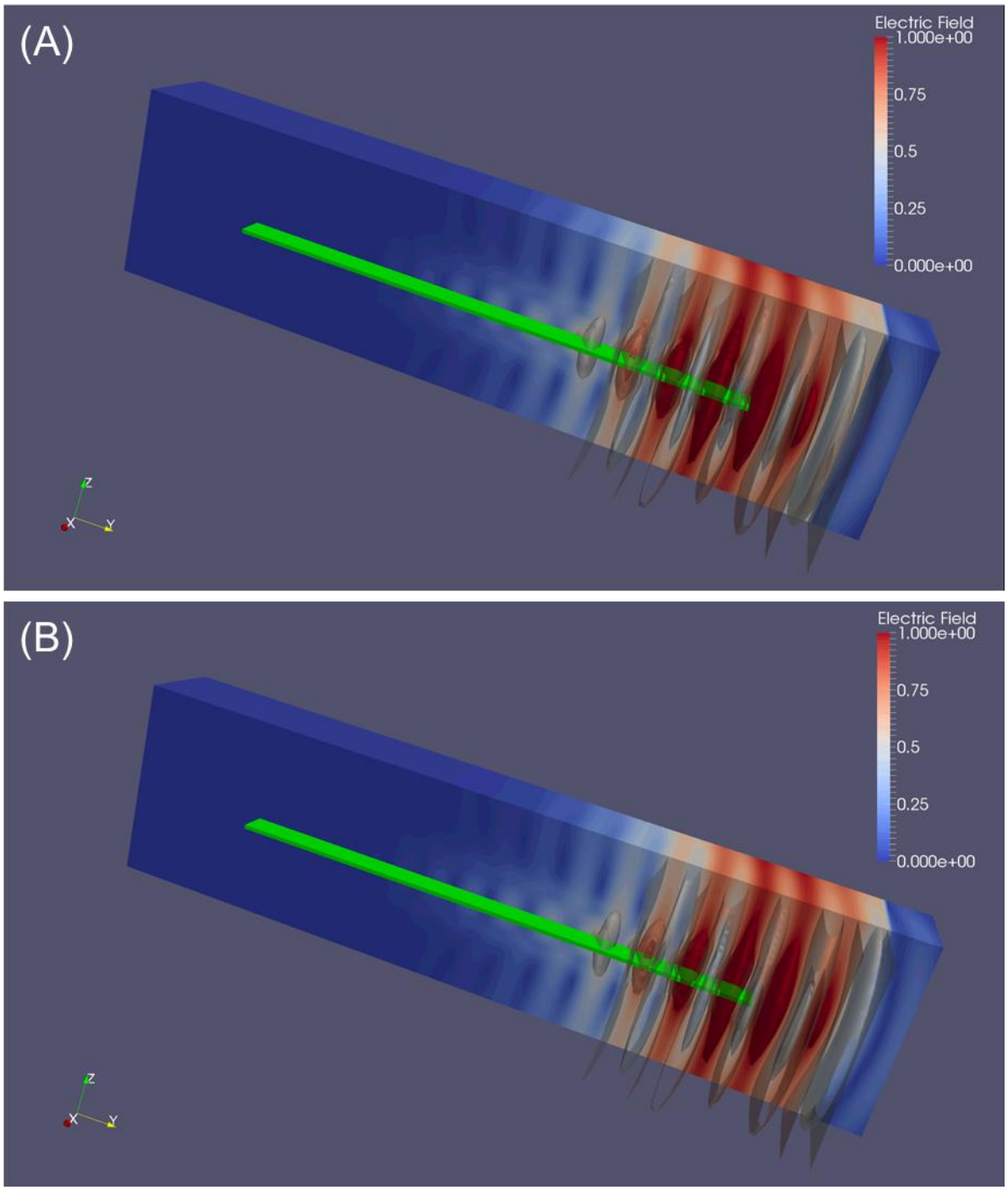

fig. S18. EFI movie snapshots. Electric field isosurface movie (EFI) snapshots with (**A**) LCP and (**B**) RCP irradiation upon an achiral nanoribbon. The dimensions of the semiconductor achiral ribbon, are analogous to those of the helix, with a length, width and height of 2600 × 312 × 25 nm^3.

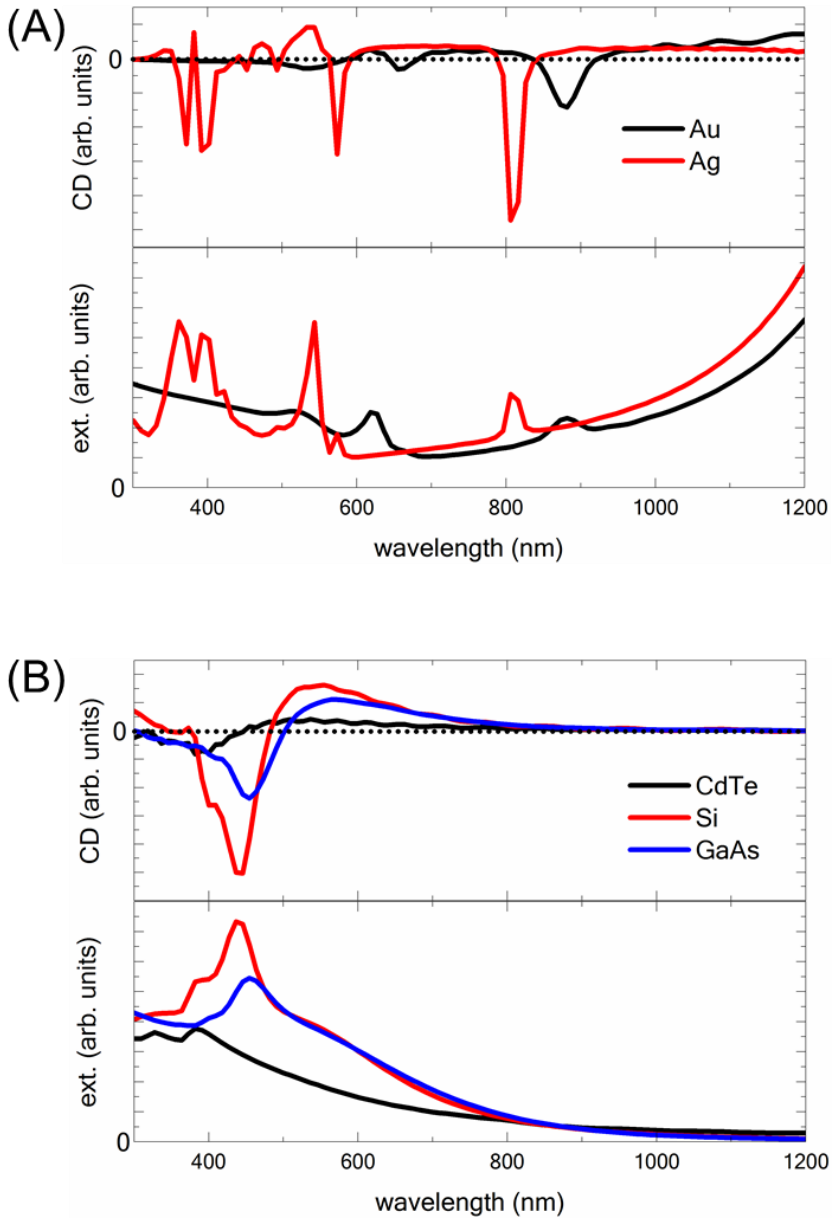

fig. S19. Nanorod dimer simulations. (**A**) Simulated CD and extinction spectra of Au and Ag nanorod dimers. (**B**) Simulated CD and extinction spectra of CdTe, Si and GaAs nanorod dimers.

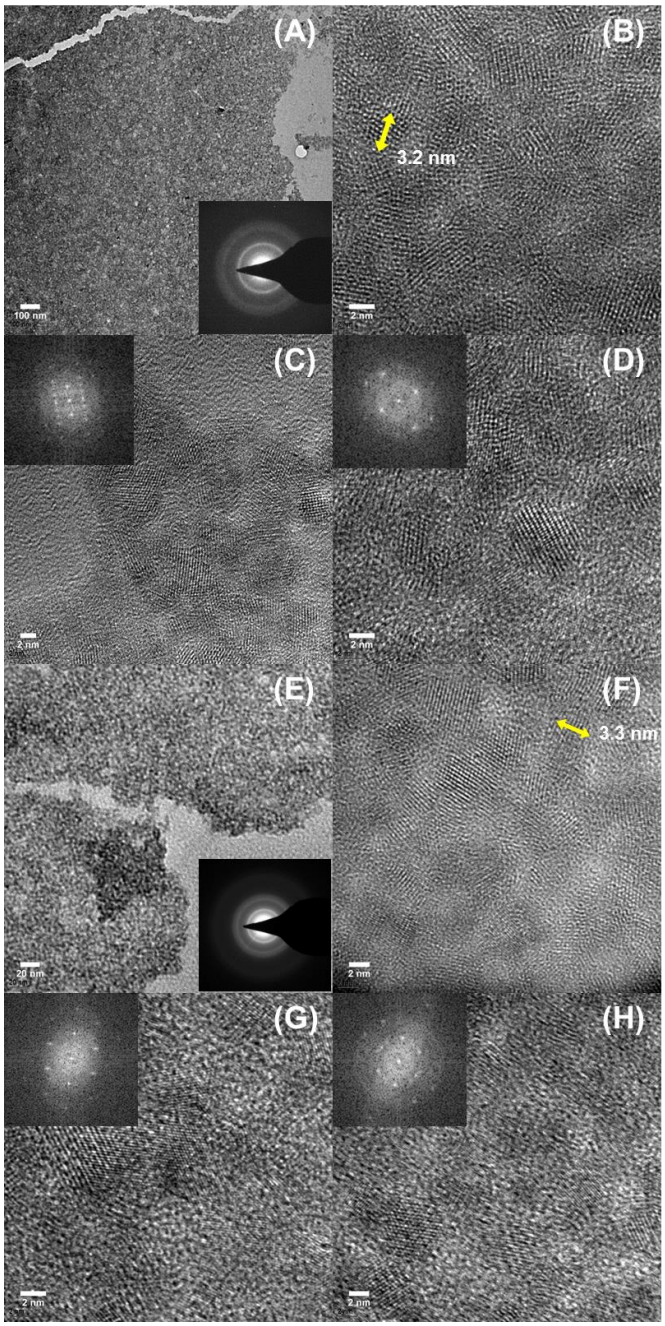

fig. S20. TEM images and crystal lattice of CdTe NPs. TEM image of D-Cys CdTe NPs at (**A**) low magnification, (**B**) high magnification, (**C**) with electron diffractogram corresponding to a [100] hexagonal structure (also possible to index as a twinned cubic structure), and (**D**) with electron diffractogram corresponding to a [211] cubic structure. TEM images of L-Cys CdTe NPs at (**E**) low magnification, (**F**) high magnification, (**G**) with electron diffractogram corresponding to a [111] cubic structure, and (**H**) with electron diffractogram corresponding to a [110] cubic structure.

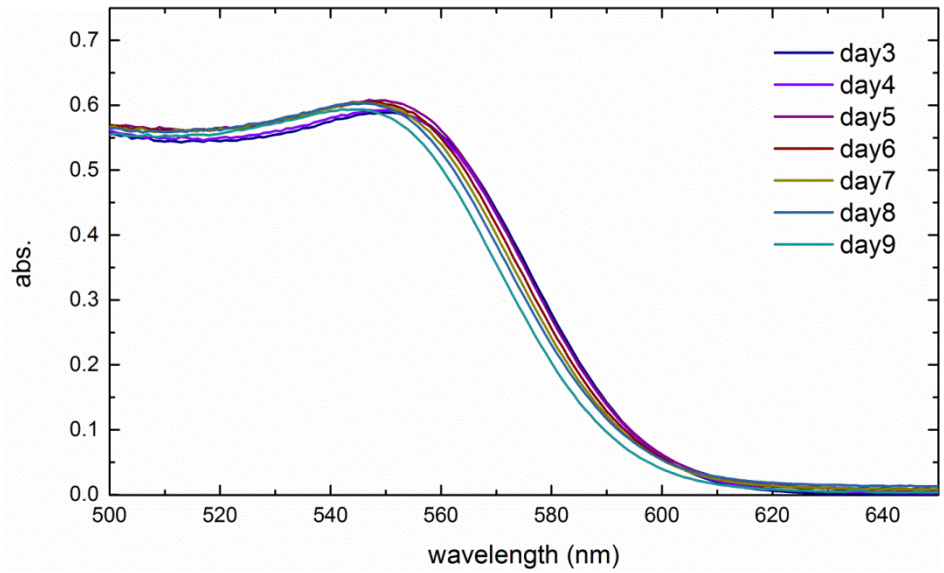

fig. S21. Absorption spectra of CdTe NPs during aging. UV-vis absorption spectra of D-Cys CdTe NPs over the course of six days.

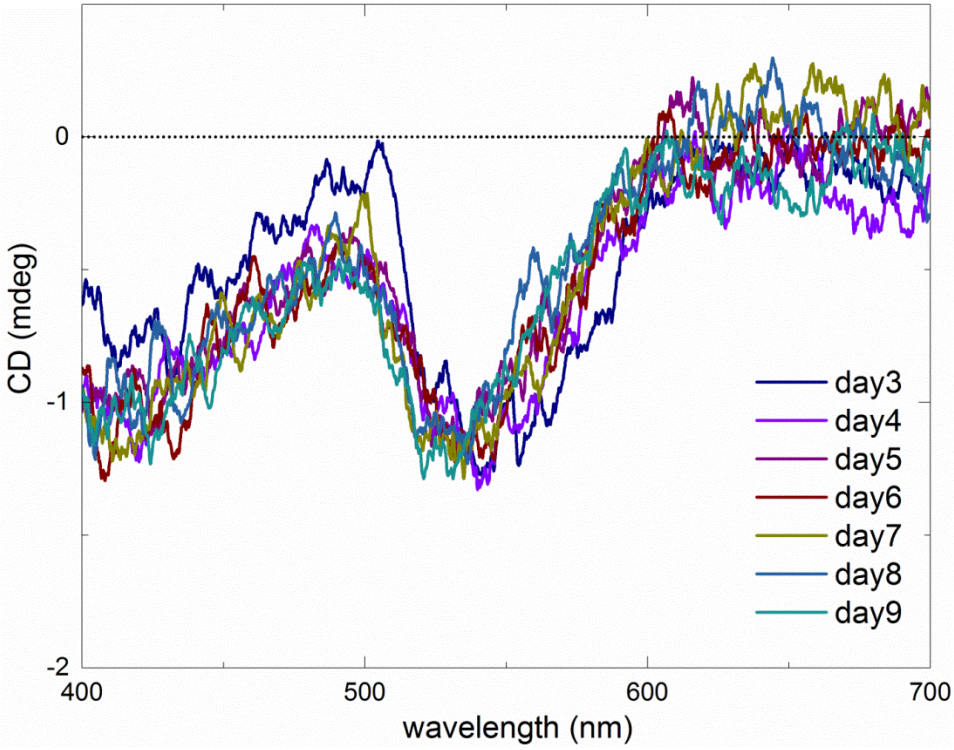

fig. S22. CD spectra of CdTe NPs during aging. CD spectra of D-Cys CdTe NPs over the course of six days.

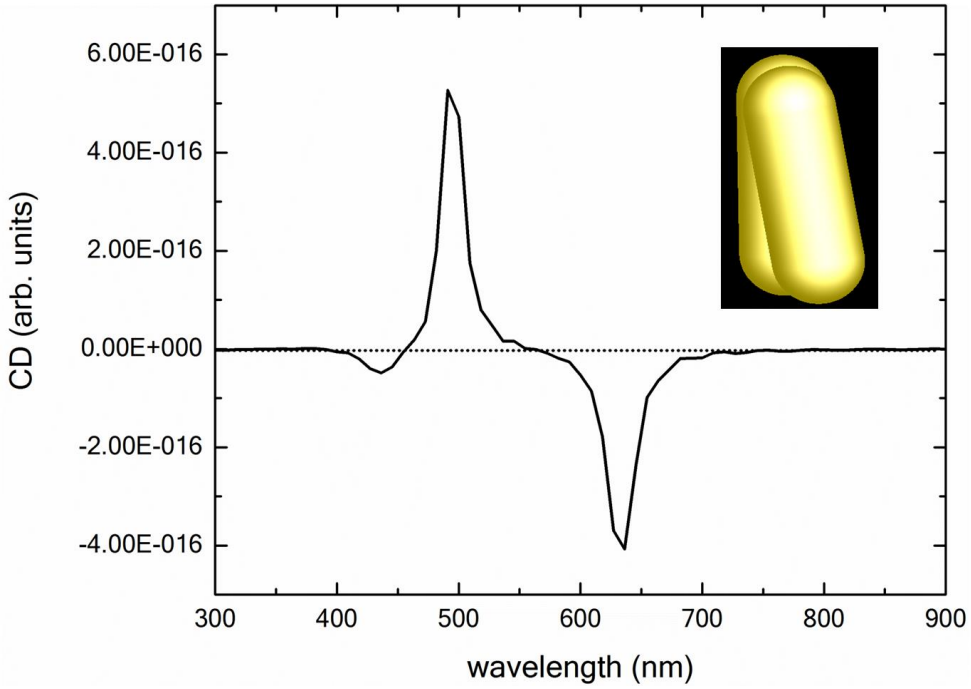

fig. S23. Verification of the computational model. Both the positive-negative bisignate spectral shape and the wavelength region match up well with the reported experimental CD spectrum.

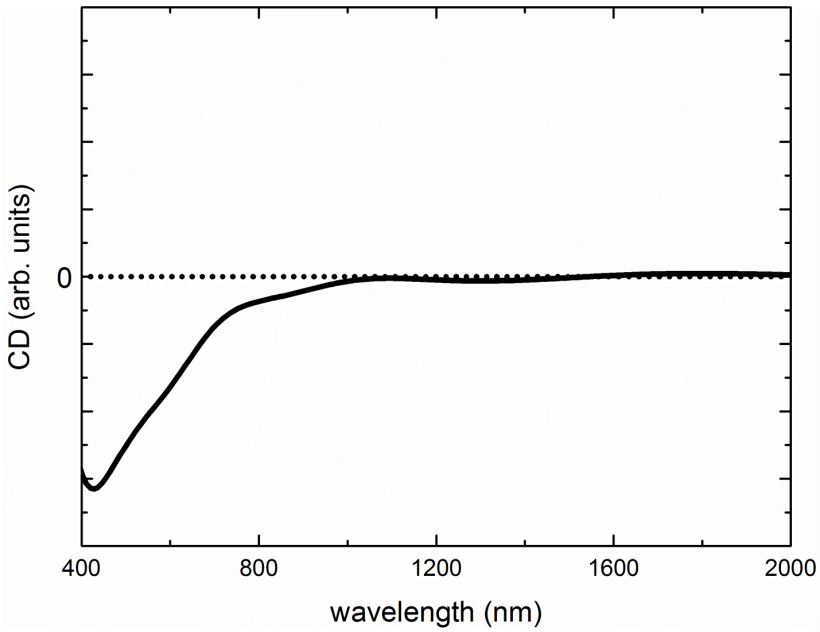

fig. S24. Simulations using CdTe NP refractive index. Simulated CD spectrum of an R-helix using CdTe NP refractive index (dataset supplied by Dr. Evren Mutlugun).

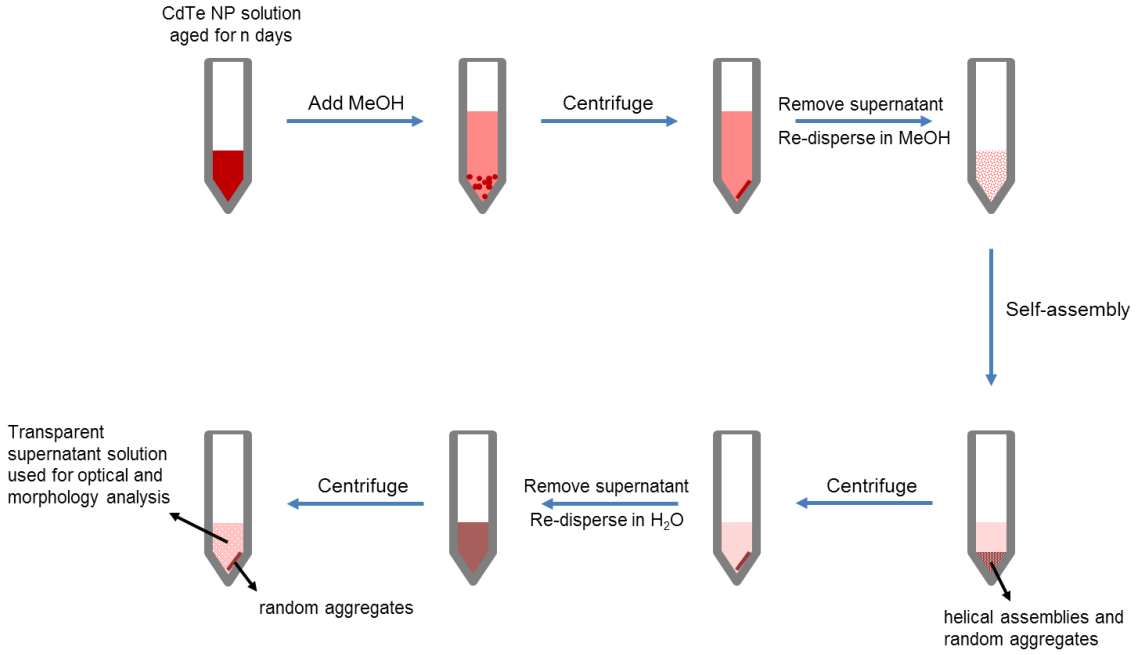

schematic S1. Experimental methods. Preparation of helical assemblies in Eppendorf vials.

table S1. Statistical analysis of racemic NP assemblies.

	L-helices	R-helices	Helices e.e.	NPs e.e.
Racemic by Synthesis	56	53	0.028	0
Racemic by Mixture	84	74	0.063	0.068

The number of helices is obtained by counting from SEM images taken at random regions of the dropcast sample.

$$Helices\ e.e. = \frac{abs_{L-helices} - abs_{R-helices}}{abs_{L-helices} + abs_{R-helices}}$$

NPs e.e is obtained by comparing the UV-vis absorbance of D-Cys and L-Cys CdTe NPs with the same 4 times of dilution:

$$NPs\ e.e. = \frac{abs_L - abs_D}{abs_L + abs_D} = \frac{0.63 - 0.55}{0.63 + 0.55} = 0.068$$

table S2. Statistical analysis of geometrical parameters of helices obtained from SEM images.

	Length (nm)	Diameter (nm)	Pitch (nm)	# of Pitches	Thickness (nm)	Corresponding Figures
D-Cys helices	2580±343	312±46	604±53	~4 (2580/604≈4)	25	fig. S14, Fig. 5A
L-Cys helices	2541±750	299±64	674±168	~4 (2541/674≈4)	37	fig. S15, Fig. 5A,5C
L-Cys helices	1176±224	257±35	<1176	~0.5	72	fig. S16, Fig. 5C

Movies

movie S1. R-helix in 3D rotating view.

movie S2. L-helix in 3D rotating view.

movie S3. RCP irradiation on an R-helix.

movie S4. RCP irradiation on an L-helix.

movie S5. RCP irradiation on an achiral ribbon.

movie S6. LCP irradiation on an achiral ribbon.

*Note: For **Movies S3-S6**, three isosurfaces were displayed (0.50, 0.71 and 0.91 V/m). The other isosurfaces were omitted for clarity.*

section S1. Percent yield

The percent yield for D-Cys and L-Cys CdTe assemblies is estimated to be the ratio of the number of NPs incorporated in all helices (N_p) and the number of original NP (N_p*). To obtain N_p, we dropcast 3 μL of helices solution onto a silicon shard for SEM imaging. We randomly selected 30 regions (each with a surface area of 0.01368 mm^2) and determined the amount of helices appearing in these areas by manual counting. Taking into account of the entire droplet surface area, we estimated the number of helices (N_h) in each 3 μL droplet. Separately, 30 images of random individual helices were taken with the intention of obtaining their average length (l) and diameter (⌀) using ImageJ analysis software. We assumed a constant thickness of

25 nm for all helices. Because of the tapered shape of the helices, the volume of an "untwisted" helix is considered to consist of three cuboids and two triangular prisms at the ends. Based on this structural assumption, the volume of a helix (Vh) = $\frac{3}{4} \times l \times \emptyset$.

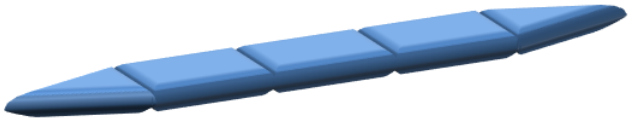

schematic S2. Schematic drawing of an "untwisted" helix

The size of the NPs is 3.2 nm. As CdTe NPs are tetrahedral in shape, the volume of a NP is $\frac{3.2^3}{6\sqrt{2}}$ = 3.86 nm^3. The average number of NP per helix ($N_{a,p}$) = $\frac{V_h}{3.86}$. The number of NP in all helices (N_p) = $N_{a,p} \times N_h$.

The absorbance of a 4-times-diluted L- and D-CdTe NP solution is 0.63 and 0.55, respectively. Together with the NP size (3.2 nm), the original NP concentration can be estimated to be 1.28E+19 per liter and 1.12E+19 per liter, for L- and D-CdTe NPs respectively. For 3 μL solution, the number of original L- and D-CdTe NPs (N_{p*}) is calculated to be 3.85E+13 and 3.36E+13, respectively.

The percent yield of helices (N_p/N_{p*}) is 0.0892% ± 0.0063% for L-Cys CdTe assemblies and 0.0944% ± 0.0038% for D-Cys CdTe assemblies. From this percent yield calculation, we see that only a small fraction of NPs self-assembled into helices, whereas the vast majority of NPs formed random aggregates. Despite the low concentration of helices in solution, the CD intensity and rotatory power of the helices remain excellent owing to their high structural chirality.

table S3. Percent Yield Calculations

	length (l)	diameter (⌀)	thickness (d)	Volume per helix (V_h)	number of nanoparticles per helix ($N_{a,p}$)	number of helices (N_h)	number of nanoparticles in all helices (N_p)	number of original nanoparticles (N_p*)	percent yield (%)	average percent yield (%)	std dev. (%)
L-CdTe 1	4380	378	25	3.10E+07	8.04E+06	4.23E+03	3.40E+10	3.85E+13	0.0884		
L-CdTe 2	4125	363	25	2.81E+07	7.27E+06	4.34E+03	3.15E+10	3.85E+13	0.0819	0.0892	0.00628
L-CdTe 3	4333	384	25	3.12E+07	8.08E+06	4.64E+03	3.74E+10	3.85E+13	0.0973		
D-CdTe 1	3443	331	25	2.14E+07	5.53E+06	5.64E+03	3.12E+10	3.36E+13	0.0929		
D-CdTe 2	3628	350	25	2.38E+07	6.17E+06	5.43E+03	3.35E+10	3.36E+13	0.0997	0.0944	0.00381
D-CdTe 3	3567	339	25	2.27E+07	5.87E+06	5.19E+03	3.05E+10	3.36E+13	0.0907		